



Metal Injection Molded Titanium: Mechanical Properties of Debinded Powder and Sintered Metal

Suparat Bootchai, Nipon Taweejun, Anchalee Manonukul, and Chaosuan Kanchanomai

(Submitted April 27, 2020; in revised form June 17, 2020; published online July 21, 2020)

Metal injection molding (MIM) is a production technique to produce small and complex titanium part. During debinding, the elements of binder may react with titanium powders, form the interstitial elements and influence the mechanical properties of sintered part. Accordingly, the chemical composition and hardness properties of commercially pure titanium, which produced by metal injection molding process, were investigated and compared with wrought commercially pure titanium. Carbon and oxygen from binder were diffused into the titanium powder during the process of debinding, i.e., the contents of carbon and oxygen and the nanoindentation hardness at the edge of powder are higher than at center of powder. After sintering, the interstitial elements formed around the pores of sintered part, which caused the higher nanoindentation hardness than that of the matrix. The yield strength and the ultimate tensile strength of sintered part were also improved because of the interstitial elements. The findings can be applied for the production, usage and development of MIM titanium.

Keywords commercially pure titanium, composition, debinding, metal injection mold, nanoindentation

1. Introduction

Metal injection molding (MIM) is an effective production technique that combines powder metallurgy with plastic injection molding technology. MIM can produce a near-net shape of small and complex metallic parts with low production cost (Ref 1, 2). Since titanium and its alloys have light weight, high strength and high fatigue resistance; they have been used in various applications, e.g., automotive, aviation, medical and dental devices (Ref 2-5).

After the injection of feedstock (i.e., a mixture between metal powder and polymer binder) into a mold, the injected parts go through the debinding process to remove the binder from the injected parts. Two main debinding processes are generally available, i.e., thermal debinding and solvent debinding. Thermal debinding is performed under a temperature-controlled environment, while the solvent debinding is performed in solvent. For MIM process of titanium and its alloys, the thermal debinding is recommended (Ref 6) because it is an environmental-friendly process, and the sintering process can be consecutively performed using a single heating profile in the same furnace. The temperature and duration of debinding are usually more than 400 °C and more than 1h dwell time, depending on the geometry of component. Under the condition

of debinding, it is possible that some elements of binder (e.g., carbon and oxygen) may react with the Ti powders to form the interstitial elements and influence the mechanical properties of MIM titanium parts (Ref 7).

Debinding mechanisms and kinetics/chemical reactions of MIM titanium were investigated by Sidambe et al. (Ref 8). It is found that leaching metal injection molded CP Ti (i.e., commercially pure titanium) in 55 °C water did not increase oxygen levels, and the titanium surfaces did not interact significantly with binder or water. Wang et al. (Ref 9) investigated the effects of solvent-thermal debinding and vacuum sintering on microstructure of MIM titanium. A hard surface layer consisting of α -Ti, TiC and TiO₂ phases was found on MIM part. Einhorn et al. (Ref 10) studied the use of binders with a water-soluble component for MIM titanium. The results showed that those binders increased the oxygen content in the sintered parts due to the incomplete removal of binders and hence adversely affected the mechanical properties. Thian et al. (Ref 11) evaluated the effects of gas flow rate and heating rate during thermal debinding on the quality of the powder injection molded Ti-6Al-4V/HA composite parts. The defect-free parts with minimal carbon level were obtained by using a slow heating rate (i.e., 20 °C/h) and a higher gas flow rate (i.e., 250 cm³/min) at the beginning of the debinding process.

Although research works related to MIM titanium and its alloys are available (e.g., Ref 7-12); none of them have been focused on the relationship between the chemical composition and the localized mechanical properties of debinded powder and sintered part. Accordingly, the understanding of the effect of debinding on chemical composition and mechanical properties of MIM titanium is far from completed. In the present work, the metal injection molded titanium (MIM-Ti) was produced from the commercially pure titanium (CP Ti) powder. The chemical compositions as well as their influence on the hardness properties of debinded powders and sintered parts were separately investigated. The nanoindentation testing with a nanoscale penetration depth (Ref 13, 14) was applied to investigate the localized hardnesses of debinded powders and sintered parts. The tensile properties of MIM-Ti and wrought Ti

Suparat Bootchai and Chaosuan Kanchanomai, Center of Materials Engineering and Performance, Department of Mechanical Engineering, Thammasat University, Pathumthani 12120, Thailand; Nipon Taweejun, Thai Tohken Thermo Co., Ltd, Chonburi 20160, Thailand; and Anchalee Manonukul, National Metal and Materials Technology Center (MTEC), Pathumthani 12120, Thailand. Contact e-mail: kchao@engr.tu.ac.th.

were compared, and the difference was discussed. The findings can be applied for the production, usage and development of MIM-Ti parts.

2. Materials and Methods

2.1 Materials

Gas-atomized CP Ti grade 2 powders (Osaka Titanium Technologies Co., Ltd., Japan) were used in the present work. It has a spherical shape with the mean diameter of 26.5 μm , as shown in Fig. 1(a). While the chemical composition is listed in Table 1, the chemical composition of powder corresponds to that of ASTM F67 (Ref 15). The as-received CP Ti powder was designated as AR powder.

CP Ti feedstock was a mixture between 65.6 vol.% of CP Ti powder and 34.4 vol.% of polyacetal-based thermoplastic

binder (i.e., C, O, N and H are the main elements of binder) (Ref 6). The preparation of CP Ti feedstock was performed using a kneader (Moriyama: DS1-5MHB) at 160 $^{\circ}\text{C}$ for 30 min. CP Ti feedstock was injected (i.e., 50-MPa injection pressure and 165 $^{\circ}\text{C}$ injection temperature) into a mold to produce an injected part (i.e., a rectangular tensile test specimen with a gage section of 3.5 \times 6.1 mm). The injected part was debinded and continuously sintered in a controlled-atmosphere furnace (Shimadzu: VHLgr20/20/23). Under argon atmosphere, the injected part was heated very slowly to 450 $^{\circ}\text{C}$, held for 1 h and cooled down to room temperature for a debinded part. The debinded powder was separated from the middle of gage section of a debinded part and designated as DB powder. To characterize the microstructures of AR and DB powders, the powders were cold mounted, polished, etched with a solution of 2 ml HF, 4 ml HNO₃ and 100 ml H₂O and observed under an optical microscope (Olympus: STM-7). Because the temperature and time during debinding are not sufficient to cause the

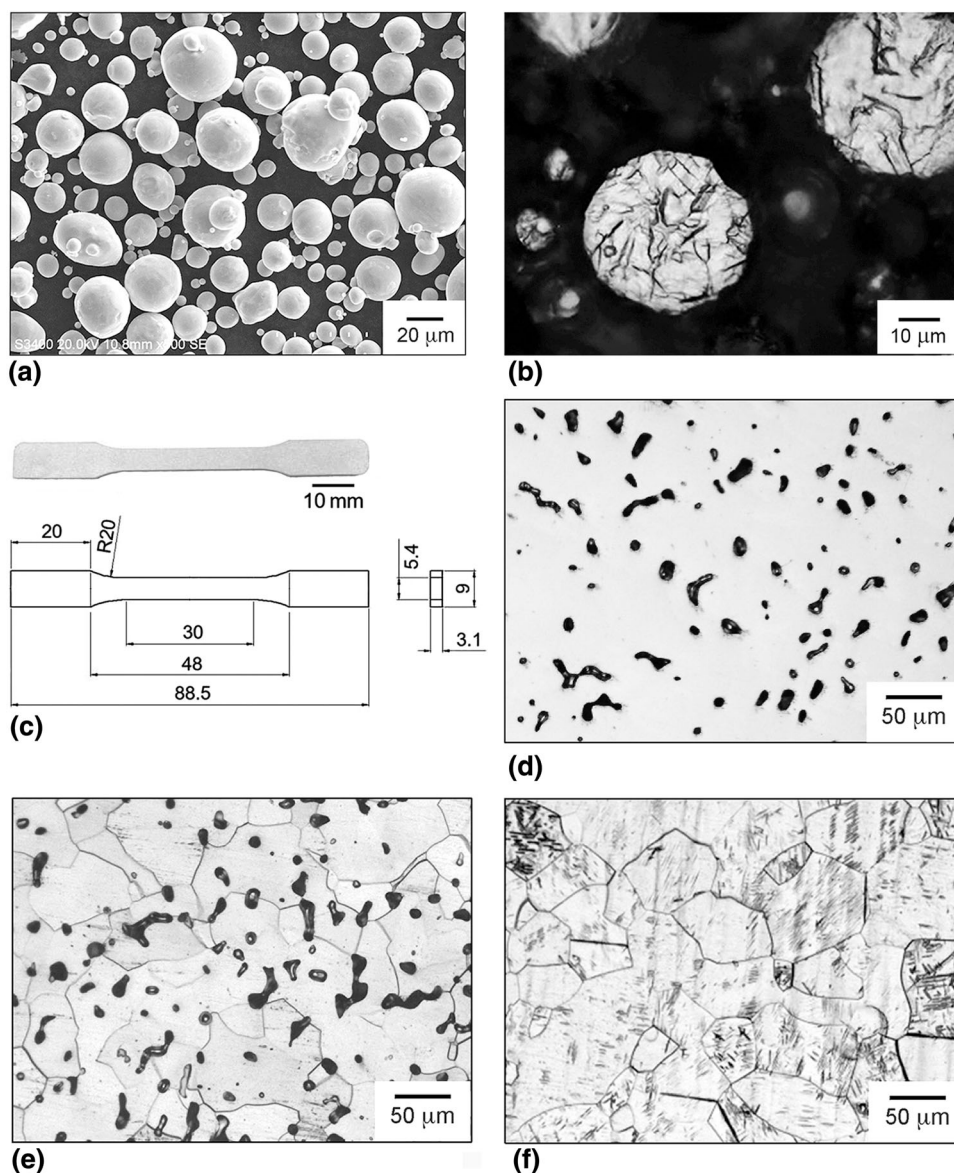


Fig. 1 Illustrations of: (a) CP Ti powder, (b) DB powder after etching, (c) sintered specimen (units are in mm), (d) MIM-Ti before etching, (e) MIM-Ti after etching and (f) w-Ti after etching

Table 1 Chemical compositions (wt.%)

Materials	C ⁽ⁱ⁾	O ⁽ⁱⁱ⁾	N ⁽ⁱⁱ⁾	Fe ⁽ⁱⁱⁱ⁾	Ti
As-received Ti powder	0.005	0.113	0.009	0.033	Bal.
MIM-Ti	0.12	0.28	0.017	0.013	Bal.
w-Ti	0.008	0.13	0.016	0.024	Bal.
ASTM F67 (CP Ti grade 2)	< 0.10	< 0.25	< 0.03	< 0.30	Bal.

⁽ⁱ⁾Infrared absorption carbon–sulfur analyzer (Leco: CS600)
⁽ⁱⁱ⁾Nitrogen–hydrogen–oxygen analyzer (Leco: TCH600)
⁽ⁱⁱⁱ⁾Inductive coupled plasma—optical emission spectroscopy (Horiba: Activa)

significant change in microstructure, the microstructural difference between AR and DB powders could not be identified. As an example, the microstructure of DB powder is shown in Fig. 1(b).

Sintering was occurred continuously in a single thermal cycle after the debinding without cooling down to room temperature. The debinded part was sintered under high vacuum environment (i.e., $< 10^{-4}$ Pa) at 1150 °C for 2 h to produce a sintered part (Fig. 1c). To obtain a specimen for the evaluation of composition and hardness, the sintered part was cut from the gage section using a wire-cut electrical discharge machining (EDM). The sintered part was designated as MIM-Ti. To evaluate the density and porosity, MIM-Ti was observed before etching (Fig. 1d) and measured using the water immersion method (Ref 16). The density, porosity and mean pore size are 4.21 g/cm³, 6.3% and 9.9 μm, respectively. To characterize the microstructure, the MIM-Ti was grounded, polished, etched and observed under an optical microscope (Keyence: VHX-6000). The grain boundaries of MIM-Ti after etching are shown in Fig. 1(e). Based on ASTM E112 (Ref 17), the mean grain size of MIM-Ti is 81 μm.

Wrought CP Ti plate (Prolog Titanium Corporation Co., Ltd., Thailand) with a thickness of 10 mm was used as a reference metal. It was annealed under vacuum environment at 650 °C for 2 h followed by furnace cooling to minimize the work hardening history of CP Ti (Ref 18). The annealed CP Ti was designated as w-Ti. Microstructure of w-Ti is shown in Fig. 1(f), i.e., 76-μm mean grain size. To obtain a specimen for the evaluation of hardness, w-Ti was cut from the annealed CP Ti plate using a wire-cut electrical discharge machining (EDM).

2.2 Chemical Composition

To investigate the effect of debinding on chemical composition of powder, a scanning electron microscope with energy-dispersive spectrometer, i.e., SEM/EDS, was applied at the center and at the surface of AR powder and DB powder. It is known that SEM/EDS is not an accurate quantitative elemental analysis method, which may include some errors from, e.g., (1) misidentification of constituent peaks, especially for minor constituents, (2) insufficient accuracy of standard analysis and (3) complex topography (Ref 19). However, SEM/EDS can be applied on a small sample (e.g., the present powder with a mean diameter of 26.5 μm), while the more accurate quantitative elemental analysis methods are required a larger sample to perform. Therefore, the operating condition of SEM/EDS was stickily controlled for each analysis before the results of AR and DB powders were used for comparative analysis.

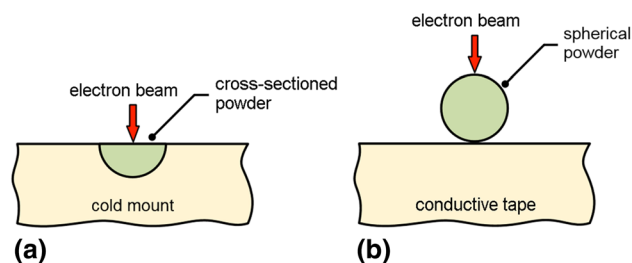


Fig. 2 Illustrations of SEM/EDS analysis: (a) at the center of cross-sectioned powder, and (b) at the surface of powder

Illustrations showing the SEM/EDS analysis of powders are shown in Fig. 2. To analyze the chemical compositions at the centers of AR and DB powders, the powders were cold mounted and polished to disclose the cross section. The mean roughness (R_a) of polished surface is approximately 0.01 μm. Subsequently, the chemical composition was evaluated using SEM/EDS (Hitachi: S-3400 N), i.e., the electron beam was applied at the center of cross-sectioned powder (Fig. 2a). On the other hand, to analyze the chemical compositions at the surfaces of AR and DB powders, the spherical powders were attached on the conductive carbon adhesive tapes. Subsequently, the electron beam was applied at the surface of powder (Fig. 2b). SEM/EDS was performed on a small area of 4×6 μm using an accelerating voltage of 20 keV. The evaluations of chemical composition at the center and at the surface were performed on 5 AR powders and 5 DB powders, and the average results were calculated.

Because a large sample can be obtained from the sintered part (i.e., approximately 3.1×5.4 mm), the more accurate quantitative elemental analysis methods can be applied for MIM-Ti and w-Ti. The bulk chemical compositions of MIM-Ti and w-Ti were evaluated using various techniques, i.e., the infrared absorption carbon–sulfur analyzer (Leco: CS600) for carbon, the nitrogen–hydrogen–oxygen analyzer (Leco: TCH600) for nitrogen and oxygen, and the inductive coupled plasma—optical emission spectroscopy (Horiba: Activa) for iron.

Under the influences of carbon and oxygen from binder, the compound phases may occur within MIM-Ti. Therefore, the formation of compound phases within MIM-Ti (i.e., around pore and at matrix) was evaluated using a soft x-ray emission spectroscopy (JEOL: JSM 7800F). At each location, the analyses were performed at 3 different points. The analysis was operated using 5 kV and 50 nA for 12.5 min. The analysis area is approximately 25 μm².

2.3 Hardness Tests

Before nanoindentation test, the powder was cold mounted and polished to disclose the cross section. The mean roughness (R_a) of polished surface is approximately $0.01 \mu\text{m}$. The hardnesses at the center and near the edge of AR powder and DB powder were analyzed and compared. According to ISO 14577-1 (Ref 20), the nanoindentation test was performed using the dynamic ultra-microhardness tester (Shimadzu: DUH-211). The indenter of nanoindentation test has a triangular-pyramid shape with 115° tip angle. All nanoindentation tests were performed under temperature of $25 \pm 2^\circ\text{C}$, and relative humidity of $60 \pm 5\%$.

During nanoindentation test, the load and displacement were recorded to create the load–displacement curve (F - h curve), as shown in Fig. 3. On the F - h curve, h_{max} is the maximum depth at the maximum load (F_{max}), while h_p is the final depth of the residual hardness impression. Based on an analysis method proposed by Oliver and Pharr (Ref 13), the indentation hardness (H_{it}) and indentation modulus (E_{it}) can be determined from the F - h curve and the projected contact area (A_p) of indentation (Ref 13, 20).

$$H_{\text{it}} = \frac{F_{\text{max}}}{A_p} \quad (\text{Eq 1})$$

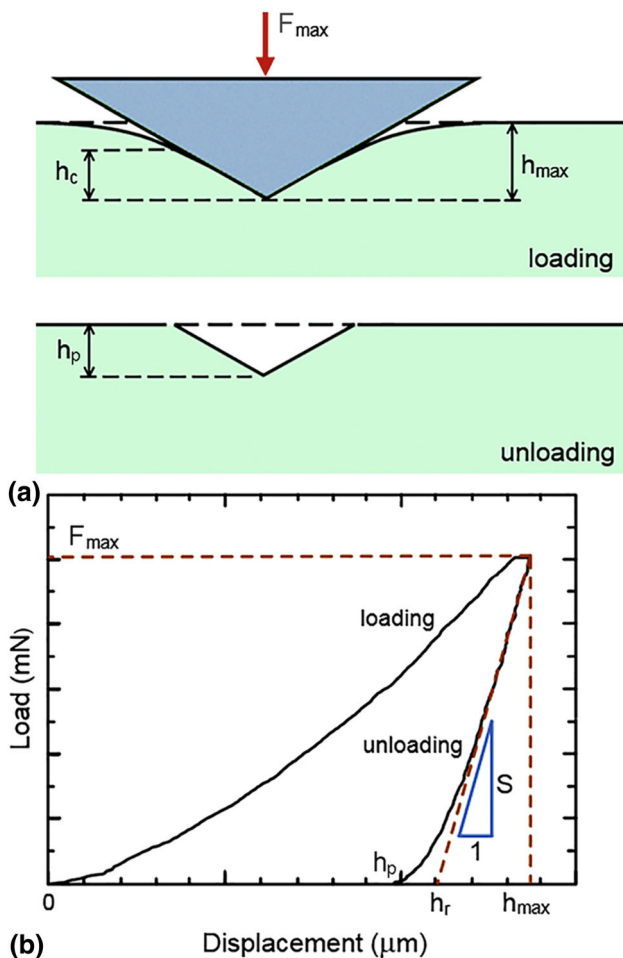


Fig. 3 Illustrations of: (a) nanoindentation mark, and (b) load–displacement curve from nanoindentation test

For shallow indentation (depth $< 6 \mu\text{m}$), the area function of the indentation cannot be assumed to be that of theoretical shape. Therefore, the Oliver’s function (Ref 13) was applied for the calculation of A_p .

$$A_p = \alpha_1 (h_c^2) + C_1 (h_c) + C_2 (h_c^{1/2}) + C_3 (h_c^{1/4}) + C_4 (h_c^{1/8}) + C_5 (h_c^{1/16}) + C_6 (h_c^{1/32}) + C_7 (h_c^{1/64}) + C_8 (h_c^{1/128}) \quad (\text{Eq 2})$$

$$h_c = h_{\text{max}} - \alpha_2 (h_{\text{max}} - h_r) \quad (\text{Eq 3})$$

where h_c is the contact depth, and h_r is the intercept of the tangent of F - h curve with the displacement axis during unloading. On the other hand, α_1 is 23.96, α_2 is 0.75, and C_1 - C_8 are the constants, which were determined by curve fitting of sample of BK7 (glass) standard material.

Indentation modulus (E_{it}) can be obtained from the slope of F - h curve at initial unloading (S), and mechanical properties of sample and indenter, as follows,

$$S = \frac{dF}{dh} = \frac{2}{\sqrt{\pi}} E_r \sqrt{A_p} \quad (\text{Eq 4})$$

$$\frac{1}{E_r} = \frac{(1 - \nu)}{E_{\text{it}}} + \frac{(1 + \nu_i^2)}{E_i} \quad (\text{Eq 5})$$

where E_r is the reduced modulus of indentation contact (i.e., the elastic deformation occurs in both the sample and the indenter during load-unload experiment), E_i is the modulus of indenter ($1.14 \times 10^6 \text{ MPa}$), ν_i is the Poisson’s ratio of the indenter ($\nu_i = 0.07$), and ν is the Poisson’s ratio of sample ($\nu = 0.33$ (Ref 18)), respectively.

Because the indentation hardness depends on the maximum load (F_{max}) (Ref 20); the various maximum loads were applied on AR powder as well as w-Ti. Then, the suitable maximum load for the investigation of the effect of debinding on the localized hardness properties of DB powder and sintered part was selected. The nanoindentation tests were performed on 4 AR powders and 6 DB powders. For each powder, the nanoindentation tests were performed at the center (6 different points) and at the edge (8 different points), and the average results were calculated. The nanoindentation technique was also used to evaluate the hardness around pore and at matrix of MIM-Ti, and compare with that of w-Ti. The sample preparation and the procedure of nanoindentation test of MIM-Ti and w-Ti were similar to those of powders. The nanoindentation tests of MIM-Ti were performed at 4 regions. At each region, the nanoindentation tests were performed around pore (6 different points) and at matrix (6 different points), and the average results were calculated.

Rockwell scale B macrohardness test of MIM-Ti and w-Ti was performed at 980-N applied load and 10-s holding time (Ref 21) using a Rockwell hardness test machine (Affri: 206RT). While the microhardness test of MIM-Ti and w-Ti was performed at 2-N applied load and 11-s holding time (Ref 22) using a microhardness machine (Future tech: FM-800). Both hardnesses were taken from 5 different points on each sample, and the average value was calculated.

2.4 Tensile Test

In accordance with ASTM E8M (Ref 23), the tensile tests of MIM-Ti and w-Ti were performed using an universal testing machine (Instron: 5969). The tensile testing specimen (Fig. 1c) was loaded under constant deformation rate of 10 mm/min, temperature of 25 ± 2 °C and relative humidity of $60 \pm 5\%$. The deformation was measured using an extensometer attached on the specimen's gage length, while the tensile force was measured using a 50-kN load cell. Subsequently, ultimate tensile strength (UTS), yield strength (YS) at 0.2% strain offset, Young's modulus and elongation were calculated.

3. Results and Discussion

3.1 Chemical Composition

3.1.1 As-Received and Debinded Titanium Powders. To perform an SEM/EDS comparative analysis, the carbon content of AR powder was used as the reference; then the ratios between the carbon content of DB powder and the carbon content of AR powder were determined, i.e., the ratio of carbon content. Similar comparative analysis was applied for the content of oxygen, i.e., the ratio of oxygen content. At the centers of powders, the ratios of carbon content and oxygen content of AR powder and DB powder are similar (Fig. 4a). On the other hand, at the surface of powders, the ratios of carbon content and oxygen content of DB powder are significantly higher than those of AR powder, as shown in Fig. 4(b). During the debinding, the diffusions of carbon and oxygen from the binder to the center of powder are unlikely. However, it is speculated that the debinding temperature and time are high and long enough to cause the diffusions of carbon and oxygen from the binder to the near-surface region of powder.

There is also another possibility that causes the increase in carbon and oxygen contents at near-surface region of DB powder, such as the contaminations of the furnace and/or the vacuum pump system. To investigate this possibility, the AR powders were subjected to the debinding cycle. Then, SEM/EDS was applied at the center and at the surface of the powder. The contents of carbon and oxygen of these powders are similar to those of AR powders. It is indicated that the contaminations of the furnace and/or the vacuum pump system are unlikely to be the source of the increase in carbon and oxygen contents at near-surface region of DB powder.

3.1.2 Wrought and Metal Injection Molded Titanium. Bulk chemical compositions of MIM-Ti and w-Ti were evaluated and compared, as shown in Table 1. The carbon, oxygen, nitrogen and iron contents of w-Ti correspond to those of ASTM F67 (Ref 15). However, the nitrogen and iron contents of MIM-Ti satisfy ASTM F67 (Ref 15), but the carbon and oxygen contents of MIM-Ti are higher. The carbon content of MIM-Ti is 20% higher, while the oxygen content of MIM-Ti is 12% higher. Because the sintering was performed under high vacuum environment, i.e., $< 10^{-4}$ Pa; carbon and oxygen from environment are minimized and should not be the main contribution of carbon and oxygen pickups during sintering. It is likely that the higher carbon and oxygen contents of MIM-Ti come from the binder, which diffuse into the powder during debinding.

With the carbon and oxygen contents near the surface of DB powder, the interstitial solid solution and/or compound phases may form after sintering, especially around pores of MIM-Ti (i.e., the incomplete bonding at the junction of DB powders). Based on Ti-C and Ti-O phase diagrams (Ref 24), the sintering temperature, and the carbon and oxygen contents, the formation of compound phases is unlikely, and only the α -titanium with small content of interstitial solid solution is expected around pores. The speculation is confirmed by the soft x-ray emission spectroscopy results (Fig. 5), which show no peaks of TiC, Ti_2O_3 , Ti_6O_{11} around pore and at matrix of MIM-Ti.

3.2 Hardness

3.2.1 Influence of Applied Load on Indentation Hardness. Indentation hardnesses at the center of AR powder and at surface of w-Ti under various maximum loads are shown in Fig. 6(a) and (b), respectively. The indentation hardness decreases with the increase in the maximum load and eventually becomes stable without the influence of the maximum load (i.e., > 20 mN for AR powder and > 400 mN for w-Ti). Thus, the maximum load beyond the stable indentation hardness should be used to obtain the actual indentation hardness, which represents the localized mechanical properties. The indentation hardnesses (H_{it}) are approximately 1.9 GPa and 2.4 GPa for AR powder and w-Ti, respectively. H_{it} of w-Ti is slightly lower than that of Fizan-Michel et al. (Ref 25) (i.e., 2.9 ± 0.4 GPa), where the recrystallization treatment was performed on CP Ti to obtain the small grain sizes of a few tens micrometers. Because the indentation depth from the load-displacement curve ($F-h$ curve) is required for the determina-

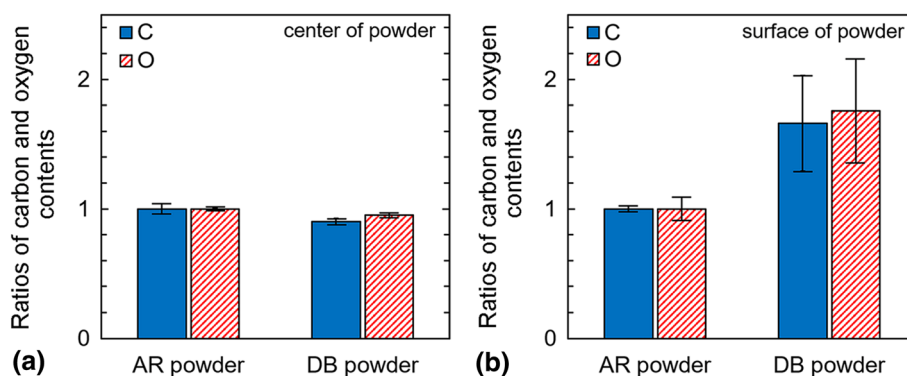


Fig. 4 Ratios of carbon and oxygen contents of AR powder and DB powder: (a) at the center, and (b) at the surface

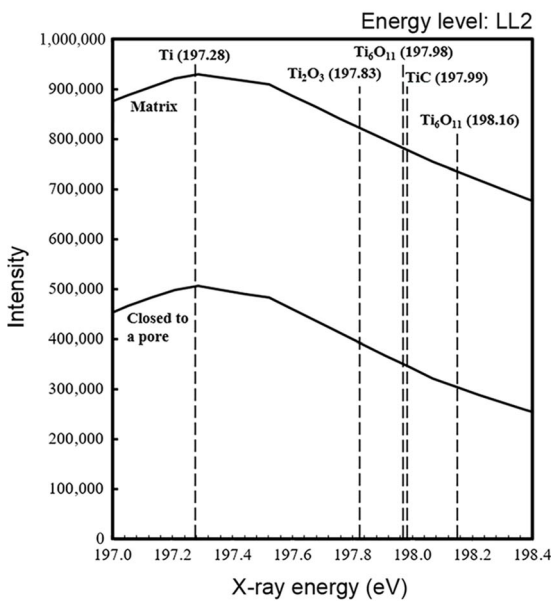
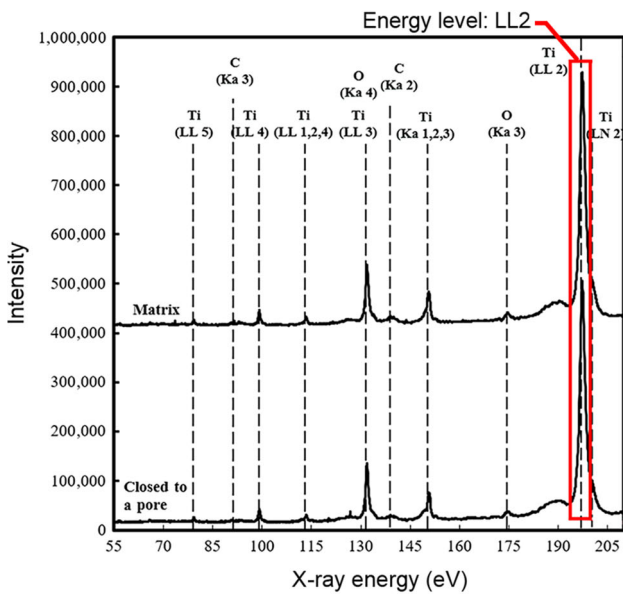
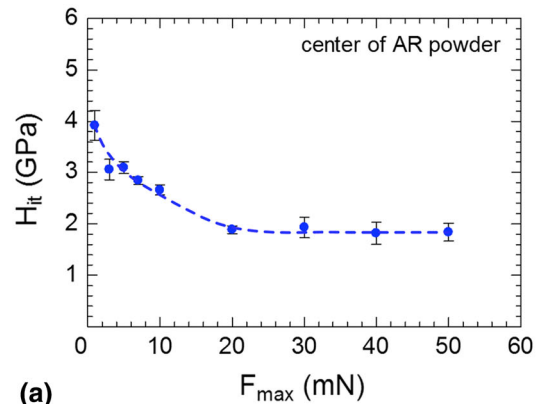


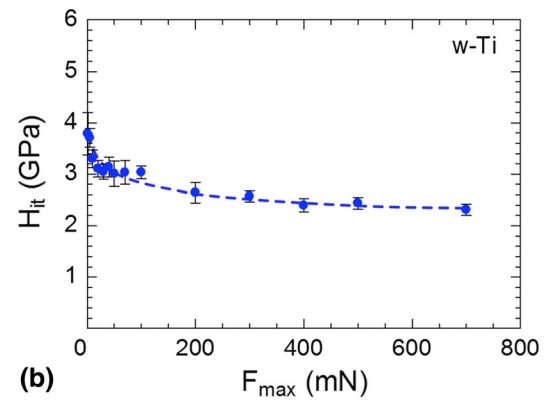
Fig. 5 Soft x-ray emission spectroscopy of MIM-Ti

tion of H_{it} ; the mount displacement of a very small sample (i.e., AR powder) may be a significant fraction of the measured displacement. Therefore, H_{it} of AR powder is slightly lower than that of w-Ti.

To investigate the effect of debinding on the localized hardness properties of DB powder, the indentation hardnesses were intended to compare between at the center and near the edge of DB powder using a small sample (i.e., a sectioned powder with the mean diameter of 26.5 μm). The application of 20 mN on a powder produced a large indentation mark of approximately 4 μm , which is too large and not suitable to investigate the localized hardnesses near the edge of DB powder and around pore of MIM-Ti. Thus, the maximum load of 5 mN with the loading/unloading rate of 0.3 mN/s (i.e., an indentation mark with approximately 1.2- μm width and 0.27- μm depth) was used for the localized hardnesses of AR powder, DB powder, MIM-Ti and w-Ti. The indentation marks at the center and near the edge of powder are shown in Fig. 7. The



(a)



(b)

Fig. 6 Indentation hardnesses as a function of the maximum loads: (a) at the center of AR powder, and (b) at the surface of w-Ti

minimum indent spacing (i.e., approximately 3 μm) corresponds to that recommended by Sudharshan Phani and Oliver (Ref 26), in which a minimum indent spacing should be 10 times greater than the indentation depth to obtain the accurate results for a Berkovich indenter. To evaluate the hardnesses around pore and at matrix of MIM-Ti (i.e., > 15 μm further away from pore), the nanoindentation technique was also performed and compared with that of w-Ti. The indentation marks on the region around pore and at the matrix of MIM-Ti are also shown in Fig. 7. Because the indentation hardness with 5 mN is not represented the actual hardness of materials, it intends to be used only for comparative analysis.

3.2.2 As-Received and Debinded Titanium Powders. Load-displacement curves of nanoindentation tests of AR and DB powders are shown in Fig. 8(a) and (b), respectively. At the centers of AR and DB powders, the load-displacement curves are almost identical, except the magnitudes of h_p are slightly different. On the other hand, near the edges of AR and DB powders, the load-displacement curves are significantly different. The finding corresponds to the speculation that the diffusions of carbon and oxygen from the binder to the near-surface region of powder may occur during debinding (Fig. 4b), which consequently cause the change in localized hardnesses.

Indentation moduli (E_{it}) at the center and near the edge of AR and DB powders are shown in Fig. 9(a). All E_{it} are similar. The modulus involves the electrostatic force that governs atomic bonding in solid; however, the small content of interstitial elements may not significantly alter the atomic bonding and modulus. Accordingly, the diffusions of carbon

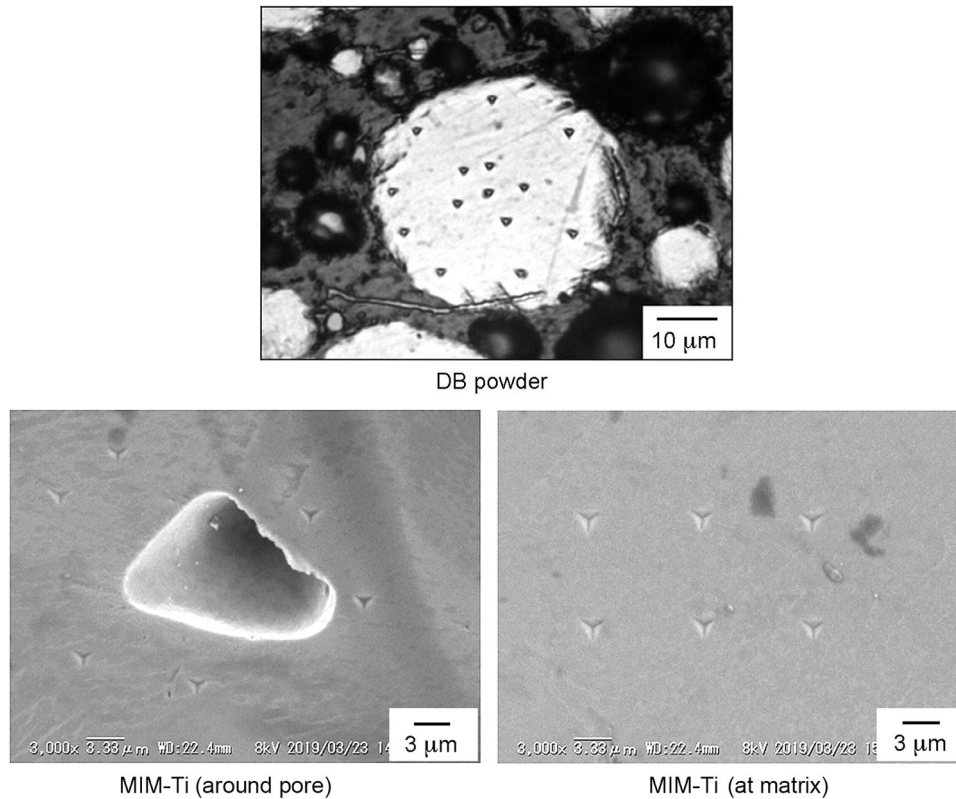


Fig. 7 Nanindentation marks on DB powder and MIM-Ti

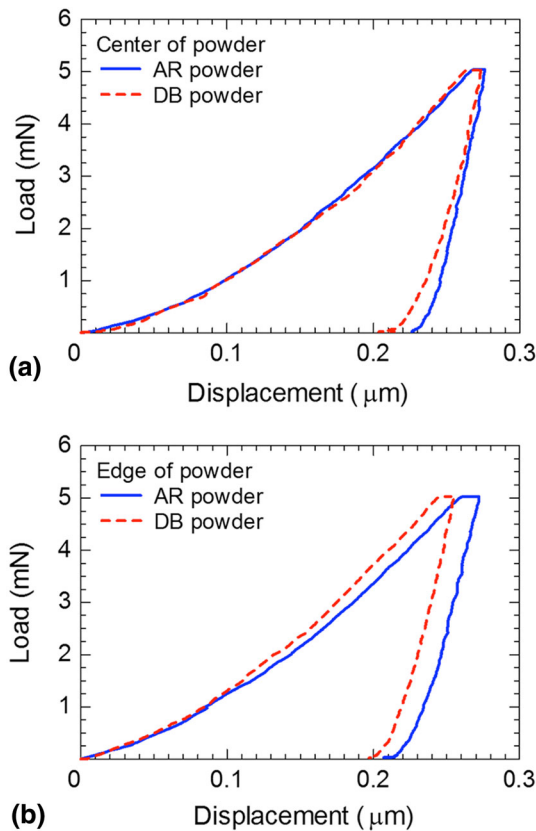


Fig. 8 Load–displacement curves of nanoindentation tests: (a) center of powder and (b) edge of powder

and oxygen from the binder to the near-surface region of powder has no impact on the modulus of DB powder.

Indentation hardnesses (H_{it}) of AR powder and DB powder at the center and near the edge are shown in Fig. 9b. H_{it} at center of AR powder and DB powder are similar. Meanwhile, H_{it} near the edge of DB powder is higher than that of AR powder. Because the α -titanium with small content of interstitial solid solution occurs in the near-surface region of DB powder, the interstitial solid solution can impede the dislocation motion (Ref 27) and result in an increase in hardness near the surface of powder.

3.2.3 Wrought and Metal Injection Molded Titanium. Load–displacement curves of nanoindentation tests of MIM-Ti and w-Ti are shown in Fig. 10. The load–displacement curve at the matrix of MIM-Ti is almost identical to that of w-Ti. However, around the pore of MIM-Ti, the load–displacement curves are significantly different from that at the matrix of MIM-Ti. The difference may relate to the deformation of pores in the vicinity of indentation mark and/or the contents of carbon and oxygen around pores of MIM-Ti (i.e., the remaining of carbon and oxygen pickups near the surface of DB powder).

Indentation moduli (E_{it}) around pore and at matrix of MIM-Ti and w-Ti are shown in Fig. 11(a). The effect of pore deformation on indentation modulus is marginal; thus, the moduli around pore and at matrix of MIM-Ti are similar, and also in good agreement with those of the present w-Ti and the fully dense CP Ti from previous works, i.e., 130 ± 7 GPa (Ref 25) and 128 ± 7 GPa (Ref 28). Accordingly, the deformation of pores in the vicinity of indentation mark is unlikely the cause of the difference in the load–displacement curves between around the pore and at matrix of MIM-Ti (Fig. 10).

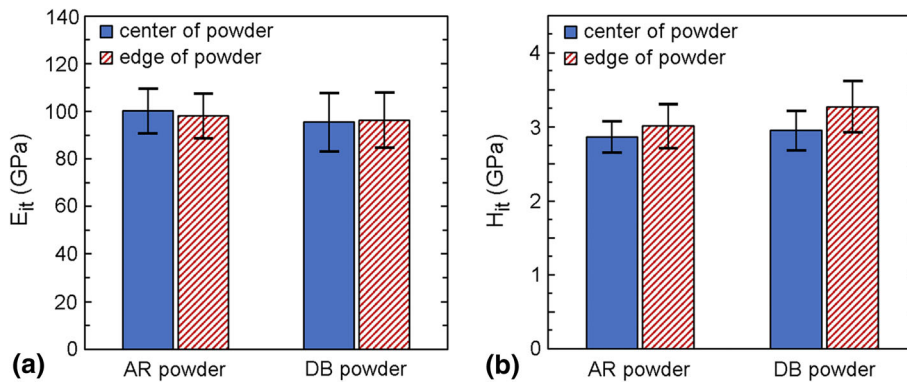


Fig. 9 AR and DB powders: (a) indentation moduli and (b) indentation hardnesses

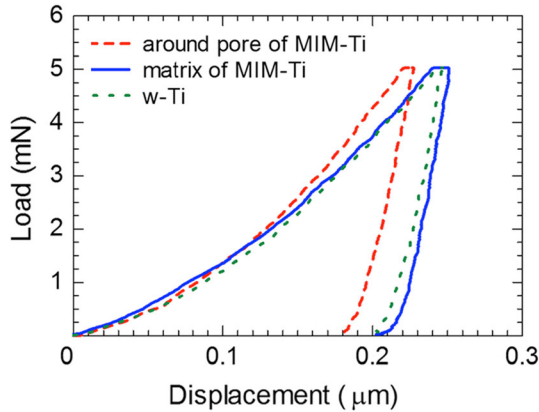


Fig. 10 Load-displacement curves of nanoindentation tests of MIM-Ti and w-Ti

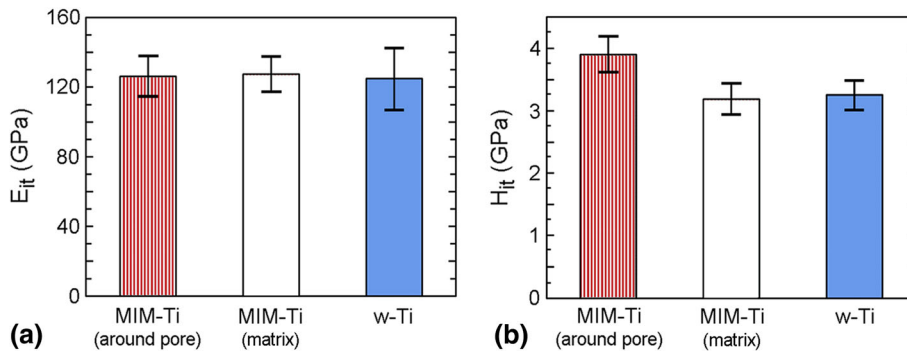


Fig. 11 MIM-Ti and w-Ti: (a) indentation moduli, (b) indentation hardnesses

Indentation hardnesses (H_{it}) around pore and at matrix of MIM-Ti and w-Ti are shown in Fig. 11(b). H_{it} at matrix of MIM-Ti and w-Ti are similar. On the other hand, H_{it} around pore is 22.6% higher than that at matrix. With the diffusions of carbon and oxygen from the binder to the near-surface of DB powder, the interstitial solid solution forms after sintering, especially around pores of MIM-Ti. This interstitial solid solution results in the higher hardness around pore than that at matrix of MIM-Ti.

Macrohardnesses of MIM-Ti and w-Ti are similar (i.e., 80.6 ± 1 HRB and 80.5 ± 0.3 HRB, respectively) and are in good agreement with that of Ti grade 2 given in ASM Handbook, i.e., 80.6 HRB (Ref 29). The microhardnesses of

MIM-Ti and w-Ti are also similar (i.e., 176 ± 14 Hv and 175 ± 7 Hv, respectively), and in accordance with the Ti grade 2 given in ASM Handbook, i.e., > 145 Hv (Ref 29). Unlike the nanoindentation test of MIM-Ti, the indentation sizes of macrohardness and microhardness (i.e., approximately 800 and 50 μm , respectively) are significantly larger than the pore size. Thus, the pore densification is expected and overcomes the positive effect of interstitial solid solution of carbon and oxygen. Therefore, the macrohardnesses and microhardnesses of MIM-Ti are nearly similar to those of w-Ti.

3.3 Tensile Properties

Tensile properties are summarized in Table 2. It is noted that the nominal cross-sectional area of tensile testing specimen was used to determine the stress. The nominal cross-sectional area at the gage part of MIM-Ti tensile testing specimen is

slightly larger than its net-solid cross-sectional area, which excludes the area of pores. Thus, the stress from the tensile test of MIM-Ti becomes lower than the actual values. Without pores, the net-solid cross-sectional area and the nominal cross-sectional area at the gage part of w-Ti tensile testing specimen are identical. Because the stress is used for the determination of modulus; MIM-Ti tensile testing specimen gives slightly lower modulus than that of w-Ti tensile testing specimen.

For porous material, the high stress (i.e., the stress concentration) is expected around pores; then the yield strength and the ultimate tensile strength of porous material should be lower than those of fully dense material (Ref 30, 31). However, the mean pore size of MIM-Ti is 9.9 μm , which is significantly

Table 2 Tensile properties of MIM-Ti and w-Ti

Samples	Young's modulus, GPa	Yield strength, MPa	UTS, MPa	Elongation, %
MIM-Ti	99	468	542	15
w-Ti	102	307	432	28

smaller than the mean grain size of 81 μm . It is likely that these pores are too small to generate the significantly high stress concentration. On the other hand, the carbon and oxygen contents within MIM-Ti are significantly higher than those of w-Ti (Table 1), which can reduce the dislocation mobility and enhance the yield strength and the ultimate tensile strength of MIM-Ti. Therefore, the yield strength and the ultimate tensile strength of MIM-Ti are higher than those of w-Ti.

For a fully dense ductile material, the reduction in load bearing area (i.e., the necking) occurs at the gage part of tensile testing specimen after the ultimate tensile stress. For MIM-Ti, the dislocation density after the ultimate tensile stress is expected to be significantly high, especially around pores. Thus, the strengthening mechanism (i.e., the reduction in dislocation mobility due to the interstitial solid solution) are no longer the dominated mechanism. Therefore, the complete fracture of MIM-Ti can occur earlier than that of w-Ti, i.e., the elongation of MIM-Ti is lower than that of w-Ti.

4. Conclusions

MIM-Ti was produced from CP Ti powder. The formation of interstitial elements as well as their influence on the hardness properties of debinded part and sintered part were investigated. The debinding under 450 $^{\circ}\text{C}$ for 1 h was enough to cause the diffusions of carbon and oxygen from the binder to the near-surface region of debinded powder, i.e., the carbon and oxygen contents at the near-surface region were higher than those at the center region. The interstitial elements at near-surface region of debinded powder caused a higher nanoindentation hardness than that at the center region. After sintering at 1150 $^{\circ}\text{C}$ for 2 h, it was found that the bulk carbon and oxygen contents of MIM-Ti are significantly higher than those of w-Ti. Because the interstitial elements formed around the pores of MIM-Ti, the nanoindentation hardness around the pores became higher than that at the matrix. The high carbon and oxygen contents within MIM-Ti enhanced the yield strength and the ultimate tensile strength, while the severe dislocation around pores after the ultimate tensile stress causes the reduction in elongation of MIM-Ti.

Acknowledgments

The authors would like to acknowledge the supports from Mr. Phanuphak Seensattayawong and Miss Viyaporn Krongtong (National Metal and Materials Technology Center, Thailand), the Thammasat School of Engineering Research Fund and the National Research Council of Thailand (NRCT).

References

1. M.R. Kamal, A.I. Isayev, and S.J. Liu. Injection Molding: Technology and Fundamentals, Hanser Publications (Cincinnati, OH), 2009
2. F.F.A. Hamidi, W.S.W. Harun, M. Samykano, S.A.C. Ghani, Z. Ghazalli, F. Ahmad, and A.B. Sulong. A Review of Biocompatible Metal Injection Moulding Process Parameters for Biomedical Applications, *Mater. Sci. Eng. C*, 2017, **78**, p 1263–1276
3. D.F. Heaney, *Handbook of Metal Injection Molding*, Woodhead Publishing Limited, Cambridge, 2012
4. A. Dehghan-Manshadi, M.J. Bermingham, M.S. Dargusch, D.H. StJohn, and M. Qian, Metal Injection Moulding of Titanium and Titanium Alloys: Challenges and Recent Development, *Powder Technol.*, 2017, **319**, p 289–301
5. M. Scharvogel and W. Winkelmueller, Metal Injection Molding of Titanium for Medical and Aerospace Applications, *JOM*, 2011, **63**(2), p 94–96
6. Y. Kankawa, Metal powder injection moldable composition, and injection molding and sintering method using such composition, US patent no. US6051184A, US Patent and Trademark Office (Alexandria, Virginia), 2000
7. R.M. German, Infrastructure Emergence for Metal Injection Molded Titanium Medical Devices, *Int. J. Powder Metall.*, 2012, **48**(2), p 33–38
8. A.T. Sidambe, I.A. Figueroa, H.G.C. Hamilton, and I. Todd, Metal Injection Moulding of CP-Ti Components for Biomedical Applications, *J. Mater. Process. Technol.*, 2012, **212**, p 1591–1597
9. R. Wang, Y. Wu, X. Zou, and C. Tang, Debinding and Sintering Processes for Injection Molded Pure Titanium, *Powder Metall. Technol.*, 2006, **24**(2), p 83–93
10. R.A. Einhorn, N.J. Amoroso, and L.E. Bogan, Novel Feedstocks for Powder Injection Molding, *Ceram. Eng. Sci. Proc.*, 1997, **18**(2), p 127–138
11. E.S. Thian, N.H. Loh, K.A. Khor, and S.B. Tor, Effects of Debinding Parameters on Powder Injection Molded Ti-6Al-4 V/HA Composite Parts, *Adv. Powder Technol.*, 2001, **12**(3), p 361–370
12. R.M. German, Progress in Titanium Metal Powder Injection Molding, *Materials*, 2013, **6**, p 3641–3662
13. W.C. Oliver and G.M. Pharr, An Improved Technique for Determining Hardness and Elastic Modulus Using Load and Displacement Sensing Indentation Experiments, *J. Mater. Res.*, 1992, **7**(6), p 1564–1583
14. N.M. Jennett, G.M. Pharr, and C.J. McHargue, Instrumented Indentation Testing in Materials Research and Development, *Philos. Mag.*, 2006, **86**(33–35), p 5153–5154
15. Unalloyed titanium for surgical implant applications, F 67, Annual Book of ASTM Standards, Vol. 13.01, ASTM, 2000
16. Determination of density of compacted or sintered powder metallurgy (PM) products, Standard 42, Standard Test Methods for Metal Powders Metallurgy Products, Metal Powder Industries Federation, 2016
17. Standard test methods for determining average grain size, E 112, Annual Book of ASTM Standards, Vol. 03.01, ASTM, 2013
18. M.J. Donachie Jr., Titanium: A Technical Guide, 2nd ed., ASM International (USA), 2000
19. D.E. Newbury and N.W.M. Ritchie, Is Scanning Electron Microscopy/Energy Dispersive X-ray Spectrometry (SEM/EDS) Quantitative?, *Scanning*, 2013, **35**(3), p 141–168
20. Metallic materials - Instrumented indentation test for hardness and materials parameters, part 1: Test method, ISO 14577-1, ISO, 2015
21. Standard test methods for Rockwell hardness and Rockwell superficial hardness of metallic materials, E 18, Annual Book of ASTM Standards, Vol. 03.01, ASTM, 2003
22. Standard test method for microindentation hardness of materials, E 384, Annual Book of ASTM Standards, Vol. 03.01, ASTM, 2016

23. Standard test methods for tension testing of metallic materials, E 8 M, Annual Book of ASTM Standards, Vol. 03.01, ASTM, 2016
24. ASM Handbook: Alloy phase diagram, Vol. 3, ASM International (USA), 1992
25. C. Fizanne-Michel, M. Cornen, P. Castany, I. Péron, and T. Gloriant, Determination of Hardness and Elastic Modulus Inverse Pole Figures of a Polycrystalline Commercially Pure Titanium by Coupling Nanoindentation and EBSD Techniques, *Mater. Sci. Eng., A*, 2014, **613**, p 159–162
26. P. SudharshanPhani and W.C. Oliver, A Critical Assessment of the Effect of Indentation Spacing on the Measurement of Hardness and Modulus Using Instrumented Indentation Testing, *Mater. Des.*, 2019, **164**, p 107563
27. E. Baril, Titanium and Titanium Alloy Powder Injection Moulding: Matching Application Requirements, *Powder Inject. Mould. Int.*, 2010, **4**(4), p 22–32
28. F.K. Mante, G.R. Baran, and B. Lucas, Nanoindentation Studies of Titanium Single Crystals, *Biomaterials*, 1999, **20**(11), p 1051–1055
29. R. Boyer, E.W. Collings, and G. Welsch, *Materials Properties Handbook: Titanium Alloys*, ASM International, Materials Park, 1994
30. F.H. Froes, S.J. Mashl, V.S. Moxson, J.C. Hebeisen, and V.A. Duz, The Technologies of Titanium Powder Metallurgy, *JOM*, 2004, **56**(11), p 46–48
31. G.C. Obasi, O.M. Ferri, T. Ebel, and R. Bormann, Influence of Processing Parameters on Mechanical Properties of Ti–6Al–4 V Alloy Fabricated by MIM, *Mater. Sci. Eng. A*, 2010, **527**, p 3929–3935

Publisher's Note Springer Nature remains neutral with regard to jurisdictional claims in published maps and institutional affiliations.